**Supporting information for**

# Orthogonal Binary Cations Arrangement Homogenizing Interfacial Coordination and Electronic Landscapes for High Performance Perovskite Solar Cells

Yansheng Chen [a, c], Wenlei Lv [a, c], Yeyong Wu [b], Chaorong Guo [a, c], Zhijie Gao [a, c], Lingying Ren [a, c], Yu Wang [a, c], Qinrong Cheng [b, *], Peng Huang [a, c, *], Yaowen Li [b, d, *]

[a] School of Materials Science and Engineering, Key Laboratory of Advanced Technologies of Materials (Ministry of Education), Southwest Jiaotong University, Chengdu, 610031, PR China.

[b] Laboratory of Advanced Optoelectronic Materials, Suzhou Key Laboratory of Novel Semiconductor Optoelectronics Materials and Devices, State Key Laboratory of Bioinspired Interfacial Materials Science, College of Chemistry, Chemical Engineering and Materials Science, Soochow University, Suzhou 215123, PR China

[c] Research Institute of Frontier Science, Southwest Jiaotong University, Chengdu 610031, PR China.

[d] Jiangsu Key Laboratory of Advanced Negative Carbon Technologies, Soochow University, Suzhou, Jiangsu 215123, PR China

E-mail: chengqinrong@163.com; phuang@swjtu.edu.cn; ywli@suda.edu.cn

## Experimental Section

### Materials

Lead (II) iodide ($PbI_2$, 99.99%) and Me-2PACz (99%) were obtained from TCI. Formamidinium iodide (FAI), methylammonium chloride (MACl, 99.5%), and methylammonium iodide (MAI) were purchased from Greatcell Solar Ltd. Solvents, including N,N-dimethylformamide (DMF, anhydrous, 99.8%), dimethyl sulfoxide (DMSO, anhydrous, 99.8%), and isopropanol (IPA, 99.5%), were acquired from J&K Scientific Ltd. Nickel oxide ($NiO_x$) and ITO glass substrates were sourced from Advanced Electronic Technology Co., Ltd., while silver was obtained from ZhongNuo Advanced Material Technology Co., Ltd. PEAI and $EDAI_2$ were purchased from Aladdin Scientific. All materials were used without further purification.

### Perovskite Solar Cell Fabrication

ITO substrates were cleaned sequentially by sonication in detergent, deionized water, acetone, and isopropyl alcohol for 20 minutes each, followed by ultraviolet-ozone treatment for 30 minutes. A $NiO_x$ solution (10 mg $mL^{-1}$ in deionized water) was spin-coated onto the cleaned ITO substrates at 2,000 rpm for 30 seconds in ambient air and annealed at 150 °C for 15 minutes. Subsequently, a Me-2PACz solution (0.8 mg $mL^{-1}$ in isopropanol) was spin-coated onto the $NiO_x$ layer at 5,000 rpm for 30 seconds and annealed at 100 °C for 10 minutes. For perovskite precursor preparation, a 1.5 M solution was formulated by dissolving 19.5 mg of CsI, 219.3 mg of FAI, 23.8 mg of MAI, and 760.7 mg of $PbI_2$ (with 10% excess) in 1 mL of DMF: DMSO (4:1 v/v) mixed solvent, yielding a composition of $Cs_{0.05}FA_{0.85}MA_{0.1}PbI_3$ with a bandgap of 1.55 eV. A

1.4 M solution was prepared by dissolving 18.2 mg of CsI, 192.6 mg of FAI, 536 mg of $PbI_2$ (with 10% excess), 131 mg of $PbBr_2$, and 23.5 mg of MABr in 1 mL of DMF: DMSO (4:1 v/v) mixed solvent, resulting in $Cs_{0.05}FA_{0.8}MA_{0.15}Pb(I_{0.76}Br_{0.24})_3$ with a bandgap of 1.68 eV. To improve crystallization and reduce bulk defects, 12.5 mol% MACl was added to the precursor solutions for all bandgaps and stirred for 2 hours. All procedures were performed in a nitrogen-filled glovebox. or 1.55 eV perovskite films, the precursor was spin-coated onto substrates with the hole transport layer at 1,000 rpm for 10 seconds, followed by 5,000 rpm for 40 seconds, with 200 μL of chlorobenzene dripped onto the film center 5 seconds before the end of spin-coating. The substrates were then annealed at 100 °C for 30 minutes.

For 1.68 eV perovskite films, the precursor was spin-coated at 1,000 rpm for 5 seconds, followed by 5,000 rpm for 30 seconds, with 200 μL of chlorobenzene added 15 seconds before the end. Annealing was conducted at 100 °C for 15 minutes.

For two-step perovskite deposition, a 1.5 M $PbI_2$ solution in DMF/DMSO (9:1 v/v) was stirred for 120 minutes, filtered, and spin-coated onto the hole transport layer at 2,000 rpm for 20 seconds. A filtered organic salt solution in IPA (FAI: MAI: MACl = 90:6.4:9 mg $mL^{-1}$) was then spin-coated at 2,500 rpm for 30 seconds at room temperature, followed by annealing at 100 °C for 25 minutes.

**Materials and device characterizations**

UV-vis absorption spectra were measured using a Shimadzu UV-1800 spectrophotometer. Sum frequency generation (SFG) spectra were acquired using a

commercial SFG spectrometer (SFGPL2230, EKSPLA Co., Lithuania). The visible and tunable infrared (IR) laser pulses were overlapped both spatially and temporally at the sample surface, with incidence angles of 60° and 55° (relative to the surface normal), respectively. The visible pump beam had a fixed wavelength of 532 nm. The IR beam was scanned across the fingerprint and functional group regions from 1000 to 3500 $cm^{-1}$. The spectral resolution of the system was 5 $cm^{-1}$. Spectra were collected under two distinct polarization combinations: ssp (i.e., s-polarized SFG, s-polarized visible, and p-polarized IR) and ppp (i.e., p-polarized SFG, p-polarized visible, and p-polarized IR). The passivated perovskite films were fabricated with a thickness of ~800 nm to ensure they were thick enough to eliminate any interference signals from the underlying substrate. XRD was acquired with a Rigaku Ultima IV diffractometer. SEM images and device cross-sections were obtained using a Zeiss Merlin Compact field-emission scanning electron microscope. XPS was performed on a Thermo Fisher ESCALab 250Xi system. AFM and KPFM were conducted using a Bruker MM8 instrument. Steady-state and time-resolved PL spectra were measured with a 420 nm picosecond laser on a PicoQuant FluoTime 300 system. PLQY was determined with 405 nm excitation under integrating sphere mode. In situ PL spectra were acquired using a QE6500 spectrometer (Ocean Optics) in a nitrogen glovebox with 355 nm excitation. Current-voltage curves (forward scan from -0.2 to 1.2 V; reverse scan from 1.2 to -0.2 V) were obtained under AM 1.5G illumination (100 mW $cm^{-2}$) using a solar simulator and Keithley 2400 source meter. EIS, SCLC, and Mott-Schottky analyses were performed with a CHI660E electrochemical workstation under ambient conditions.

Long-term operational stability was evaluated according to the ISOS-L-2I protocol. Devices were encapsulated using cover glass (1.1 mm) and NOA61 adhesive (Norland Products Inc.). The encapsulated devices were tested under one-sun equivalent LED illumination in a nitrogen-filled glovebox. Devices were biased at the maximum power point using an electronic load, with power output monitored. The test temperature was maintained at 65 °C, and the device temperature was periodically checked with a thermometer.

**Theoretical Calculations**

ESP was conducted at the B3LYP/6-31+G(d,p) level using Gaussian 09. Density functional theory calculations were performed with the CP2K package via its Quickstep module, employing a mixed Gaussian and plane-wave approach. The Perdew-Burke-Ernzerhof functional within the generalized gradient approximation was used, with dispersion corrections via Grimme's DFT-D3 method and Becke-Johnson damping. Models were based on a 7×7×3 supercell slab of $PbI_2$-terminated $FAPbI_3$ (001). For the OrthBC configuration, $PEA^+$ and $EDA^{2+}$ cations were added in a 4:1 molar ratio; ParaC and PerpC arrangements were constructed similarly for comparison. Binding energies were calculated as Eads = E(slab@molecule) - E(slab) - E(molecule).

**Supplementary Note 1**

**Space charge limited current (SCLC) measurement**

The trap density ($N_t$) of the perovskite is calculated using SCLC measurement. The $N_t$ were calculated as follows:[1]

$$N_t = \frac{2\varepsilon_r \varepsilon_0 V_{TFL}}{qd^2}$$

where $\varepsilon_0$, $\varepsilon_r$, d, and q represent the vacuum permittivity ($8.854 \times 10^{-14}$ F/cm), the relative permittivity of perovskite films, the thickness of the perovskite film (≈830 nm), and the elementary charge ($1.602 \times 10^{-19}$ C), respectively.

**Supplementary Note 2**

**Time-Resolved Photoluminescence (TRPL)**

To probe the carrier recombination dynamics in the control, reference, and target perovskite films, TRPL decay profiles were acquired and fitted using a biexponential decay model:[2]

$$Y=A_1 \exp\left(-\frac{t}{\tau_1}\right) + A_2 \exp\left(-\frac{t}{\tau_2}\right),$$

where $A_1$ and $A_2$ are the relative amplitudes of the two decay components. The fast decay time constant $\tau_1$ is associated with radiative recombination, while the slow decay constant $\tau_2$ reflects trap-assisted nonradiative recombination processes. The average carrier lifetime $\tau_{avg}$ was calculated as $\tau_{avg}=\frac{A_1\tau_1^2 + A_2\tau_1^2}{A_1\tau_1 + A_2\tau_2}$

**Supplementary Note 3**

**Calculation of the quasi-Fermi level splitting (QFLS) based on the PL quantum yield (PLQY)**

The photoluminescence quantum yield (PLQY) bears a direct correlation with the quasi-Fermi level splitting (QFLS), provided that all PL emission originates from the radiative recombination of free charge carriers in the perovskite film. This relationship can be described by the equation below:[3]

$$QFLS = QFLS_{rad} + k_B T \cdot \ln(PLQY) = k_B T \cdot \ln\left(PLQY \frac{J_G}{J_{0,rad}}\right)$$

QFLS denotes the energy difference between the electron and hole quasi-Fermi levels within the perovskite layer. $k_B$is the Boltzmann constant, and $T$ represents the temperature (set at 300 K). $J_G$, the generation current density under illumination, is approximated by the device's short-circuit current density $J_{SC}$. $J_{0,\mathrm{rad}}$, stands for the dark-radiative recombination saturation current density. According to the detailed balance at open-circuit conditions, the $J_{0,\mathrm{rad}}$ can be calculated by the following equations:

$$J_{0,rad} = e\int_0^{\infty} EQE_{Pv}(E)\phi_{BB}(E)dE$$

$$\phi_{BB}(E) = \frac{2\pi E^2}{h^3 c^2} \cdot \frac{1}{exp(\frac{E}{k_B T}) - 1}$$

In the relevant calculations, $e$ is the elementary charge, $EQE_{\mathrm{PV}}$ represents the photovoltaic external quantum efficiency, $E$ denotes photon energy, $\phi_{BB}(E)$ is the black-body radiative spectrum, $h$ is Planck's constant, and $c$ is the speed of light in vacuum. When the inverted PSCs reach equilibrium with black-body (BB) radiation at

$T$ = 300K, the external quantum efficiency (EQE) of the devices and the emitted spectral photon flux are computed. Then, by combining this with the photoluminescence quantum yield (PLQY) of samples with different passivators, the QFLS of the samples can be derived via a corresponding equation.

**Supplementary Note 4**

**Assessment of perovskite thin film decomposition via XRD**

To assess the decomposition of the perovskite films, the formation of $PbI_2$ was analyzed using XRD. A decomposition index (*K*) was calculated based on the relative change in $PbI_2$ diffraction peak intensity before and after aging. First, the ratio R of the integral value of the $PbI_2$ peak to that of the reference perovskite (100) peak is determined for each sample:

$$R = \frac{I_{(PbI_2)}}{I_{(100)}}$$

where I denote the integrated intensity of the respective diffraction peak. The decomposition index *K* is subsequently given by:

$$K = \frac{R_{(Aged)}}{R_{(Fresh)}}$$

In these equations, the subscripts fresh and aged denote the as-prepared and aged samples, respectively.

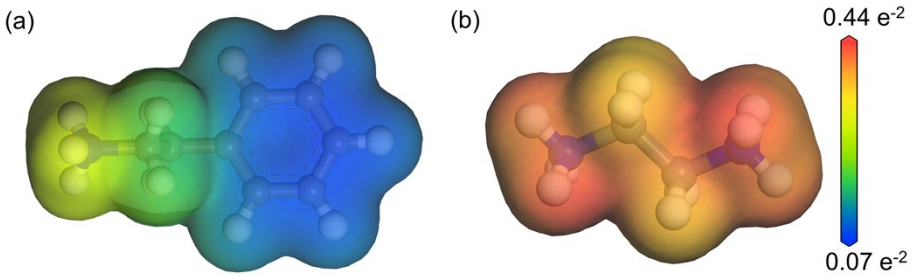


**Figure S1.** Calculated electrostatic potential (ESP) profiles of (a) $PEA^{+}$ and (b) $EDA^{2+}$ cations. The colour bar represents the fluctuation value of the ESP.

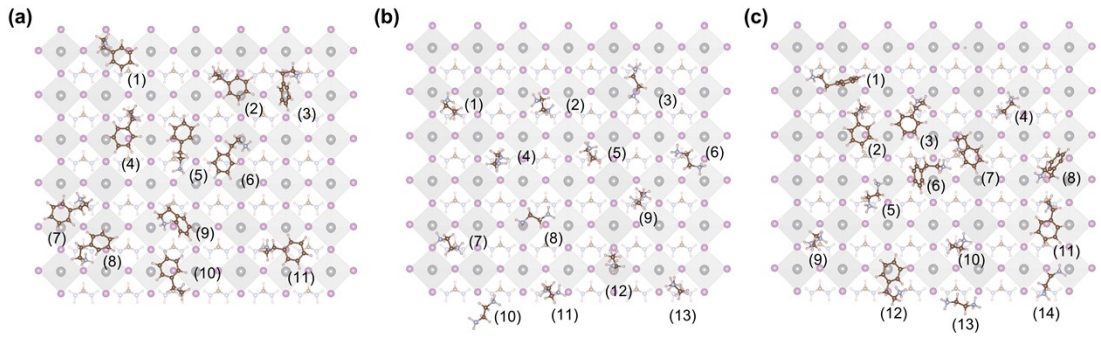


**Figure S2.** DFT-calculated top-view images of the perovskite surface with different passivators: (a) ParaC, (b) PerpC, and (c) OrthBC.

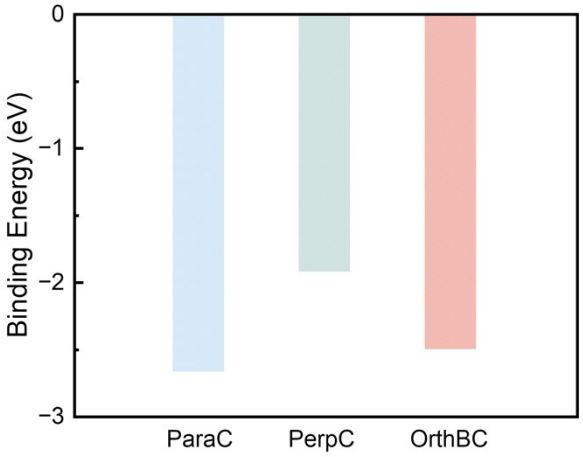


**Figure S3.** Binding energies of perovskite with different passivators.

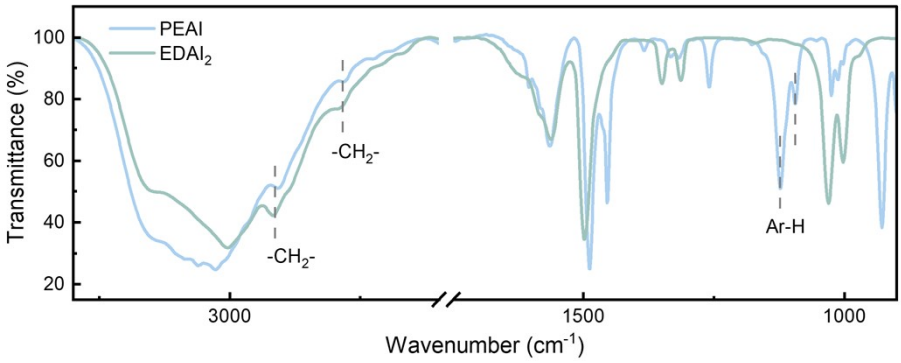


**Figure S4.** FTIR spectra of PEAI and $EDAI_2$ powders.

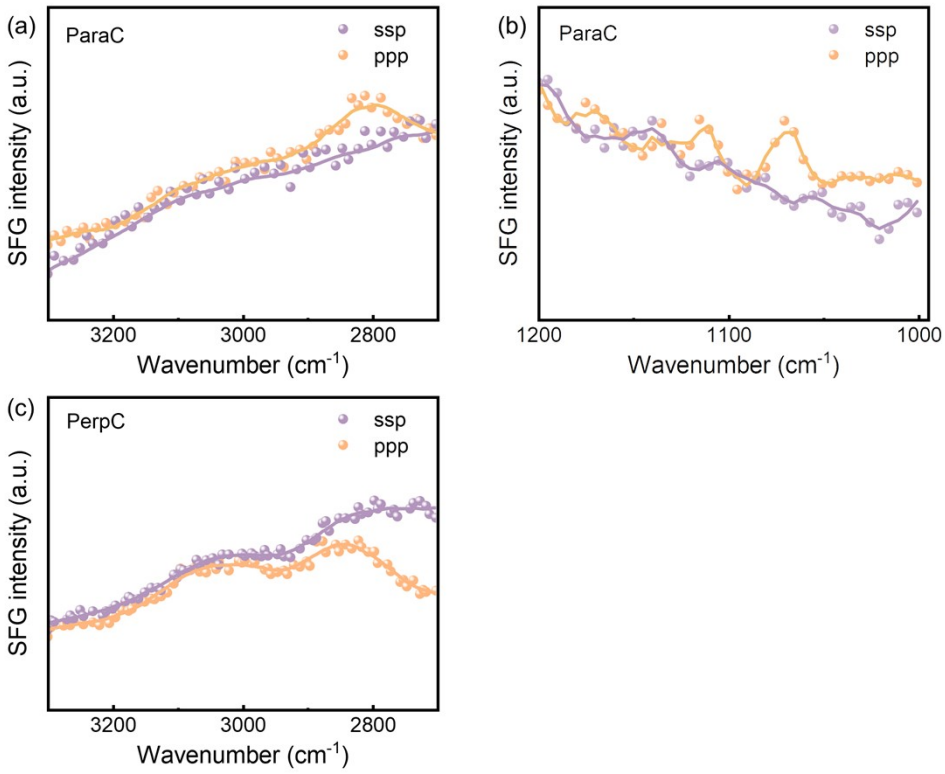


**Figure S5.** SFG spectra and corresponding fitting curves of perovskite film treated with (a, b) ParaC and (c) PerpC, respectively.

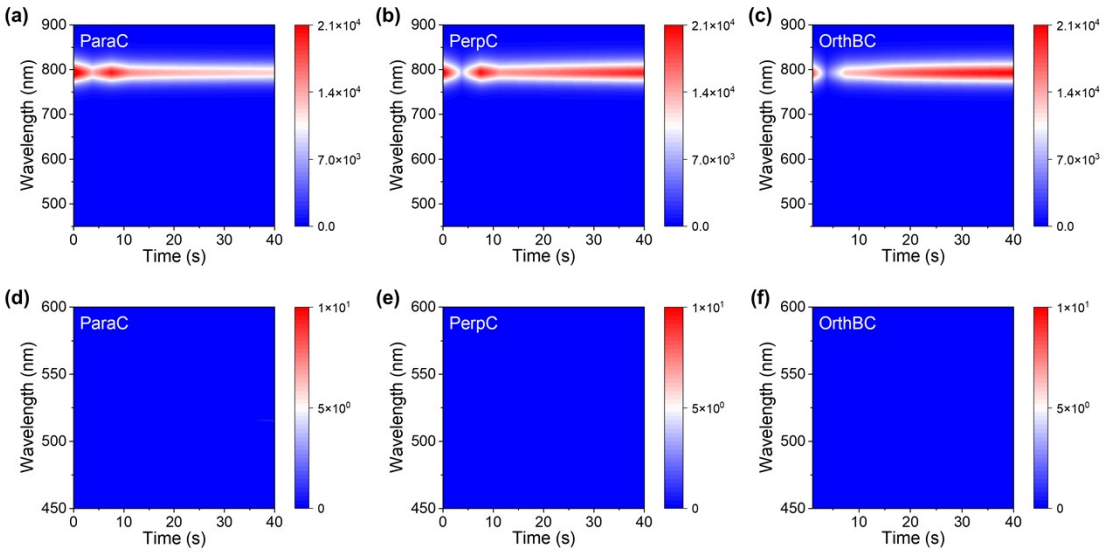


**Figure S6.** In situ PL intensity evolution of the perovskite films spin-coated with different passivators.

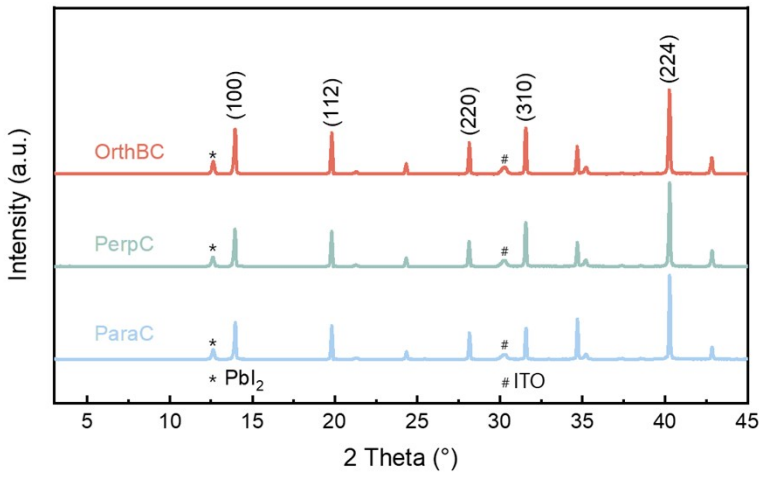


**Figure S7.** XRD patterns of perovskite films under different passivation strategies.

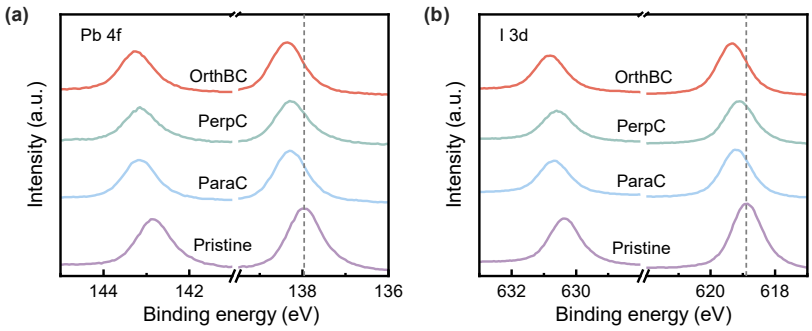


**Figure S8**. XPS core-level spectra of (a) Pb 4f and (b) I 3d for passivated perovskite films.

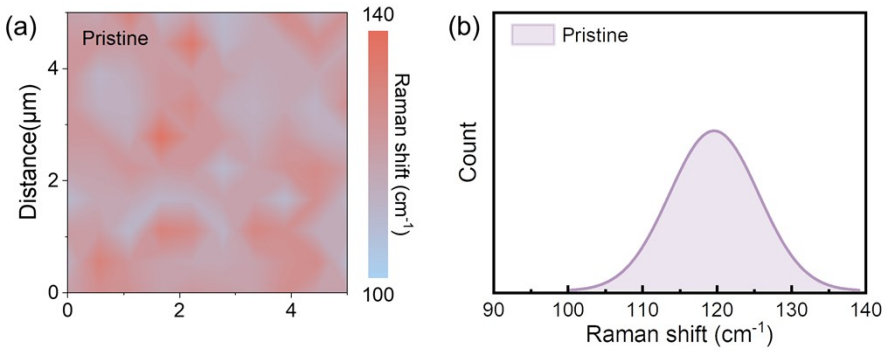


**Figure S9.** (a) Raman mapping for the Pb-I stretching vibration and (b) the corresponding spatial distribution analysis.

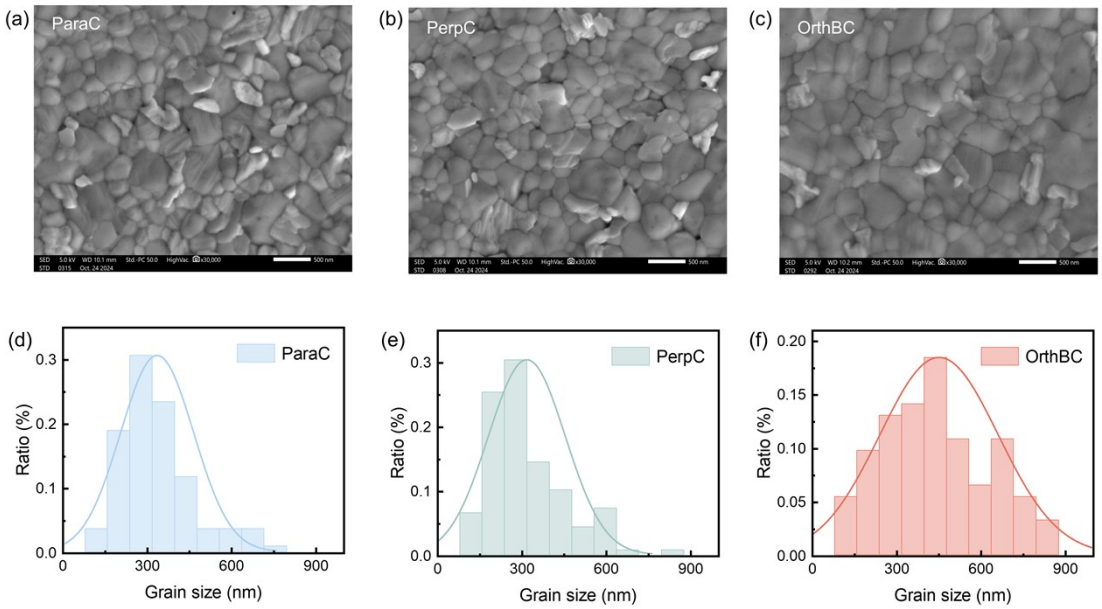


**Figure S10.** (a-c) top-view SEM images and (d-f) the quantitative analysis of grain size distribution for perovskite films with ParaC, PerpC, and OrthBC passivation.

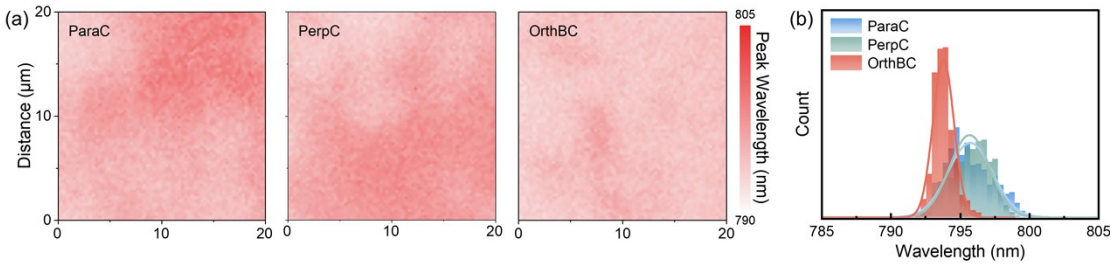


**Figure S11.** (a) PL wavelength mapping and (b) the corresponding statistical distribution.

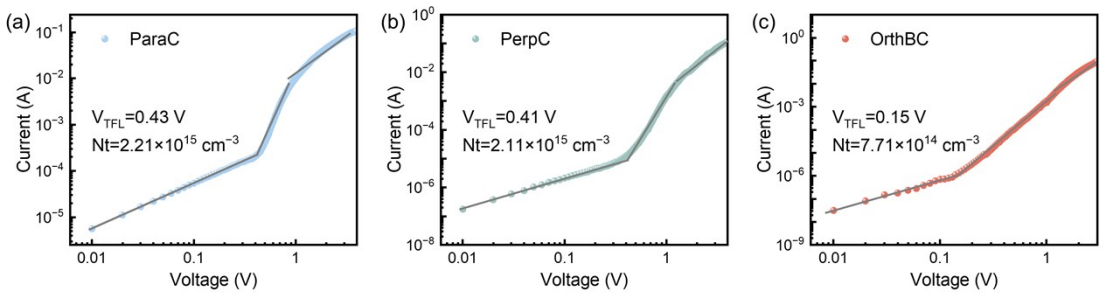


**Figure S12.** The space-charge-limited current (SCLC) measurements of electron-only devices based on perovskite films passivated with (a) ParaC, (b) PerpC, and (c) OrthBC.

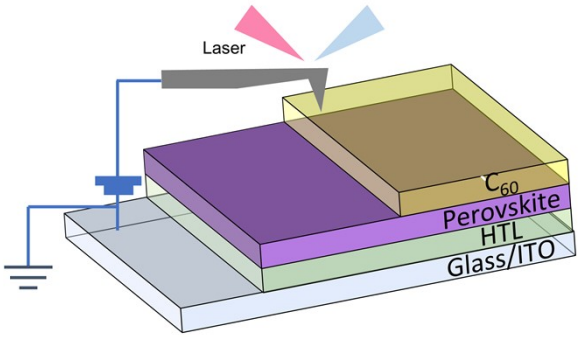


**Figure S13.** Schematic diagram of the KPFM setup used for measuring the surface potential of perovskite films that were partially covered with thermally evaporated $C_{60}$.

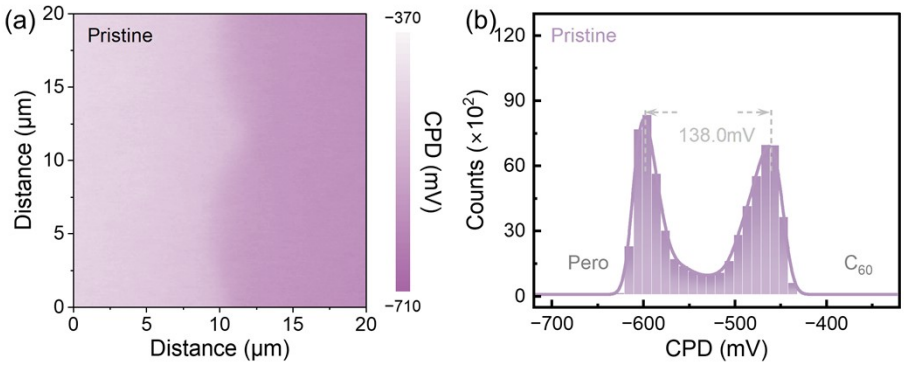


**Figure S14.** (a) KPFM potential images of perovskite/$C_{60}$ stack, along with corresponding (b) profiles of the surface potential distributions, the left region denotes the pristine perovskite, and the right region represents the $C_{60}$-coated perovskite.

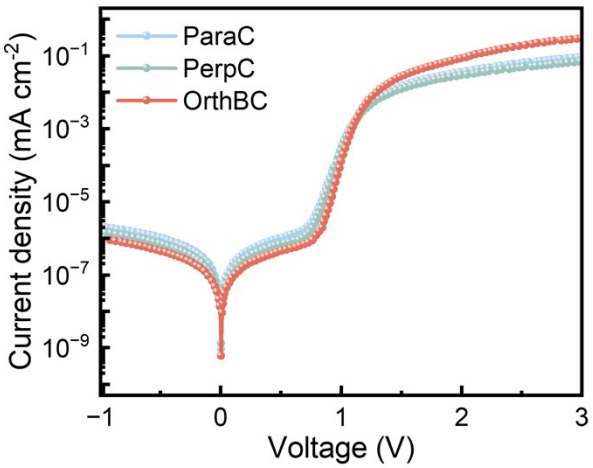


**Figure S15.** *J–V* curves of the devices measured under the dark condition.

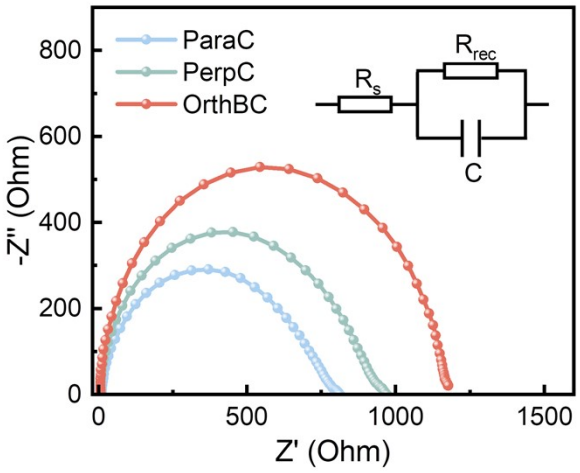


**Figure S16.** Nyquist plots of the devices. The inset is the equivalent circuit.

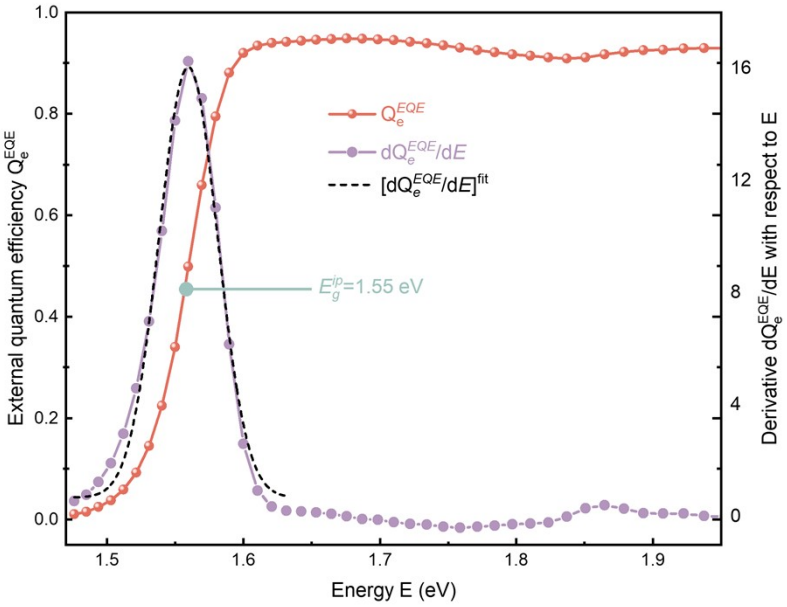


**Figure S17.** Analysis of the perovskite bandgap from the derivative of the EQE spectrum.[4]

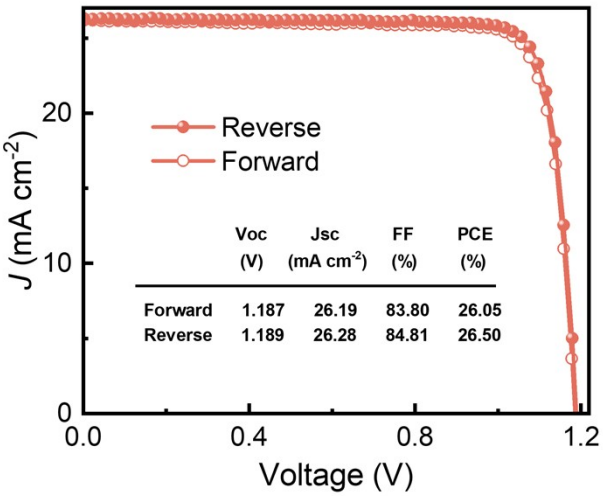


**Figure S18.** *J-V* curves of OrthBC devices under reverse and forward scan directions, with the corresponding measured PV parameters of the PSC included as an inset.

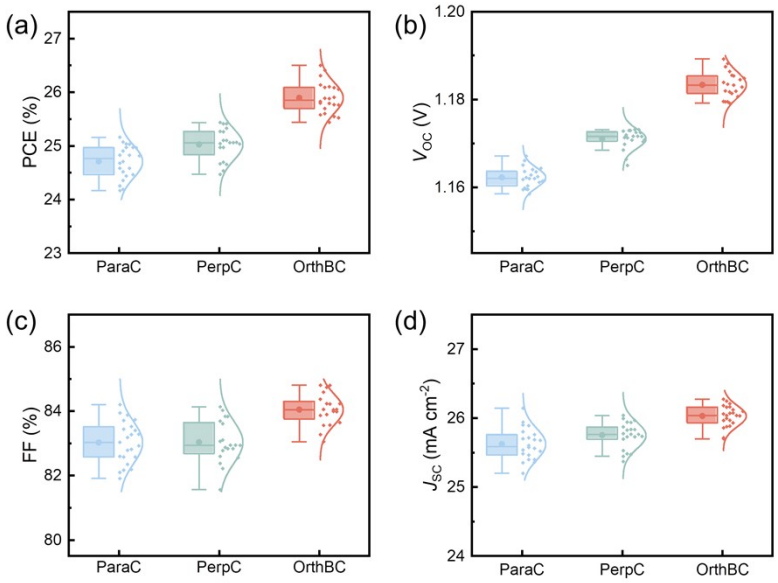


**Figure S19.** The statistical performance includes the PCE, $V_{OC}$, FF, and $J_{SC}$ of the 0.09 cm$^2$ PSCs fabricated using the antisolvent method.

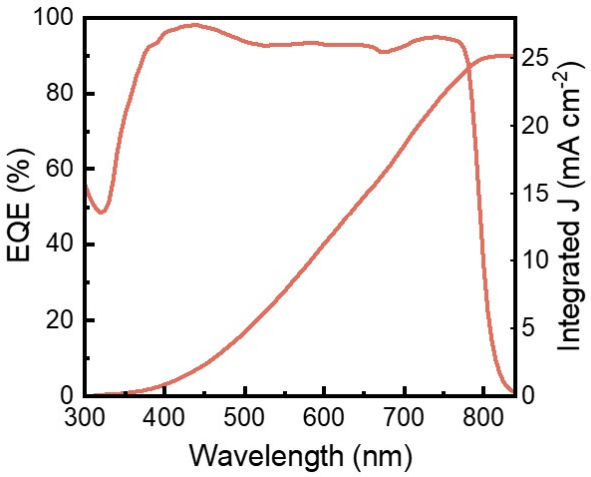


**Figure S20.** The EQE curves and the corresponding integrated photocurrent densities of the OrthBC-treated devices.

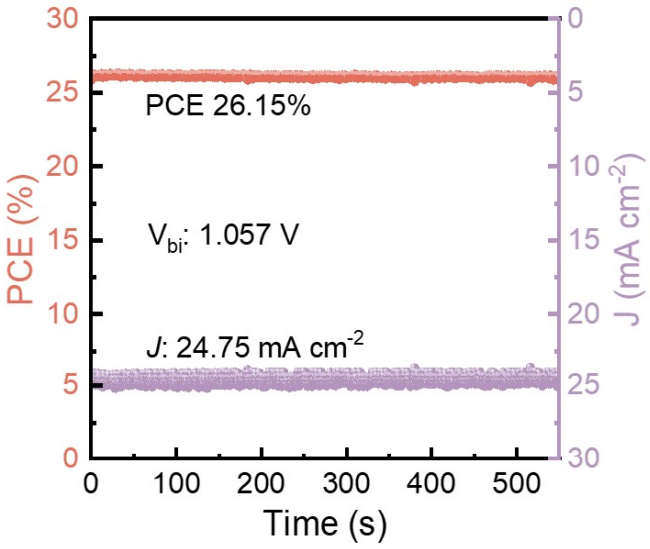


**Figure S21.** The stabilized power outputs were tested at the maximum power point of the OrthBC-treated devices.

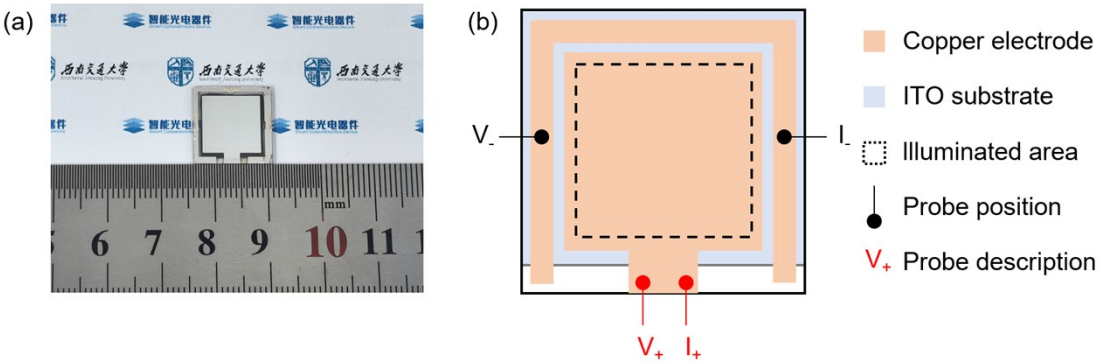


**Figure S22.** (a) Device with an effective area of 1.00 $cm^2$. (b) Schematic diagram of the four-wire measurement structure for the devices.

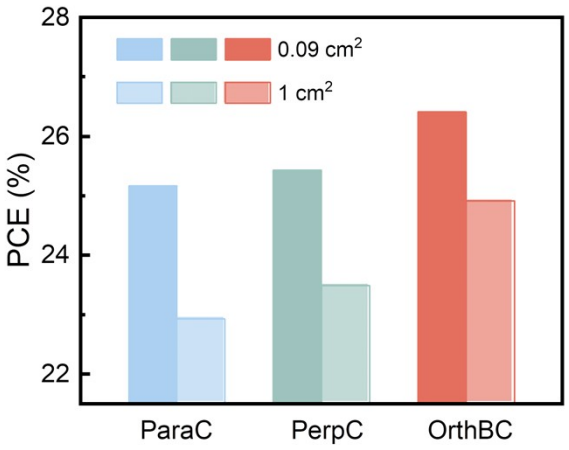


**Figure S23.** PCE comparison of devices with active areas of 0.09 $cm^2$ and 1.00 $cm^2$.

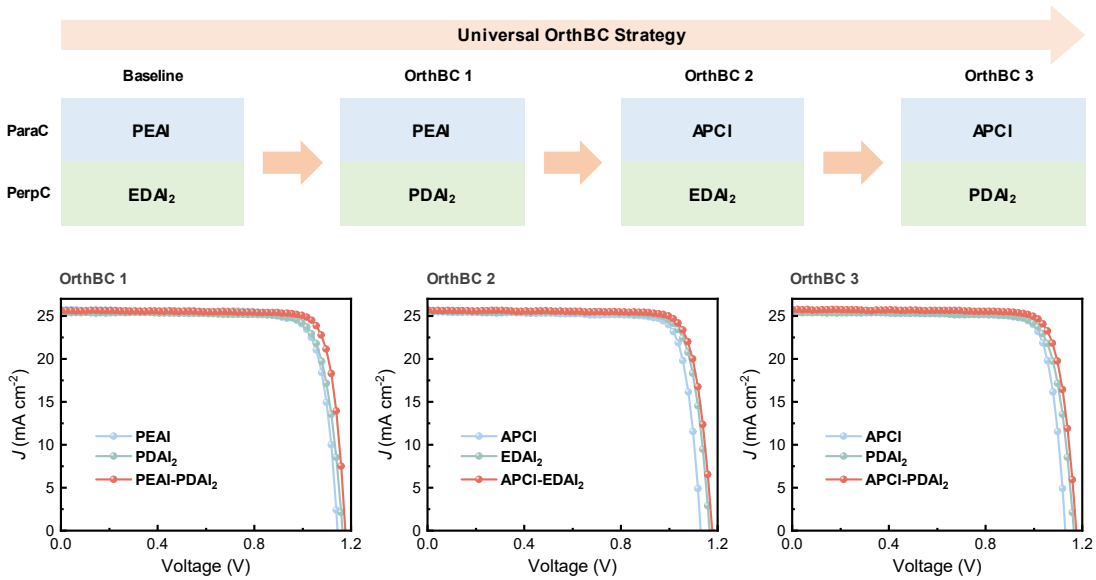


**Figure S24.** Universal applicability of the OrthBC strategy validated by *J-V* characteristics.

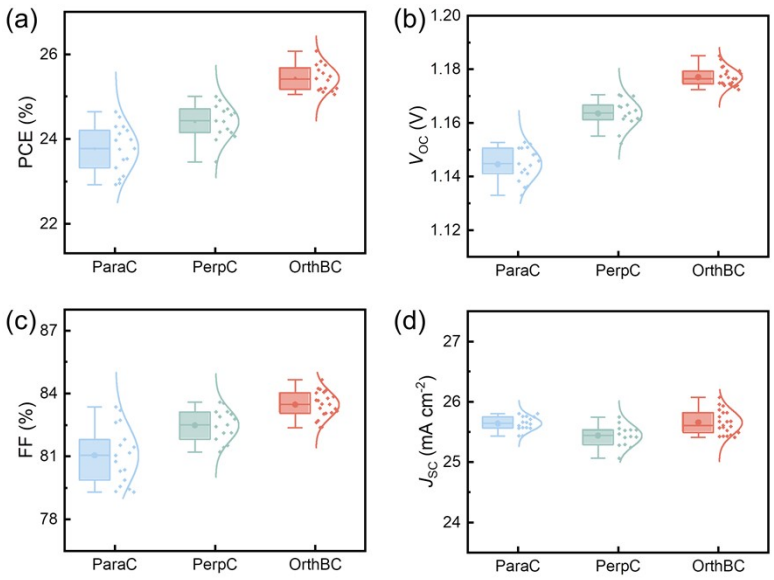


**Figure S25.** The statistical performance includes the PCE, $V_{OC}$, FF, and $J_{SC}$ of the 0.09 cm$^2$ PSCs fabricated by sequential deposition.

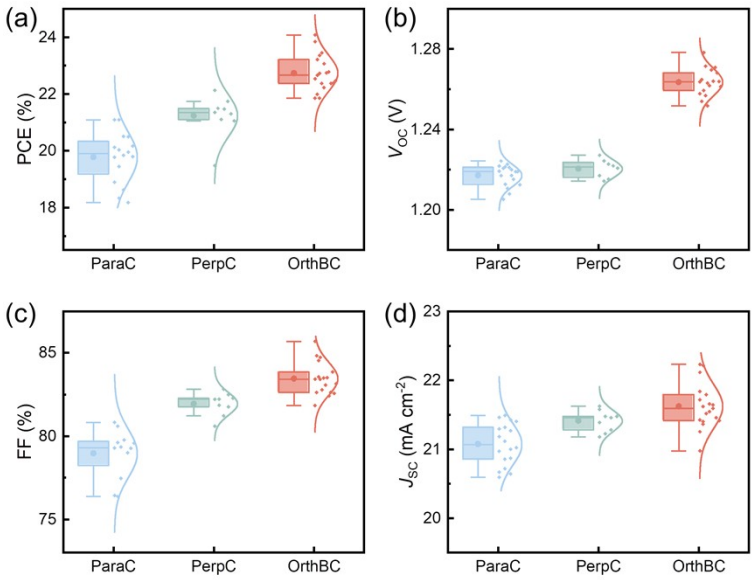


**Figure S26.** The statistical performance includes the PCE, $V_{OC}$, FF, and $J_{SC}$ of the 1.68 eV-bandgap PSCs.

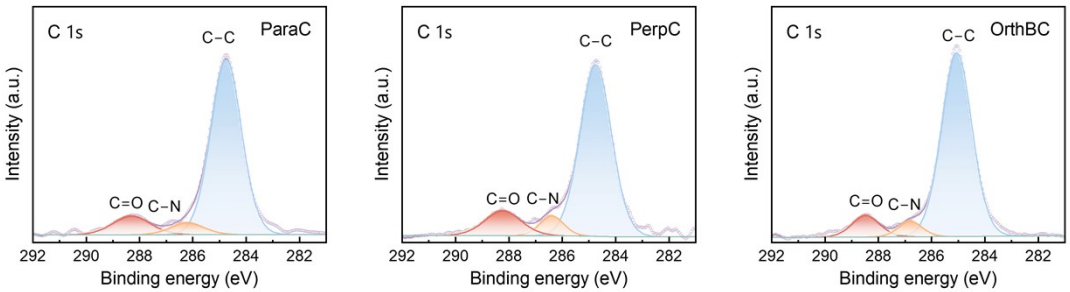


**Figure S27.** High-resolution C 1s XPS spectra of perovskite treated with different passivation strategies.

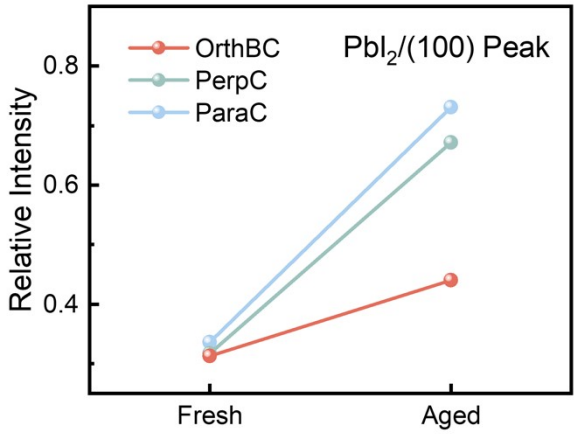


**Figure S28.** The ratio of the intensity of the $PbI_2$ peak to that of the (100) peak in the XRD pattern of the perovskite film.

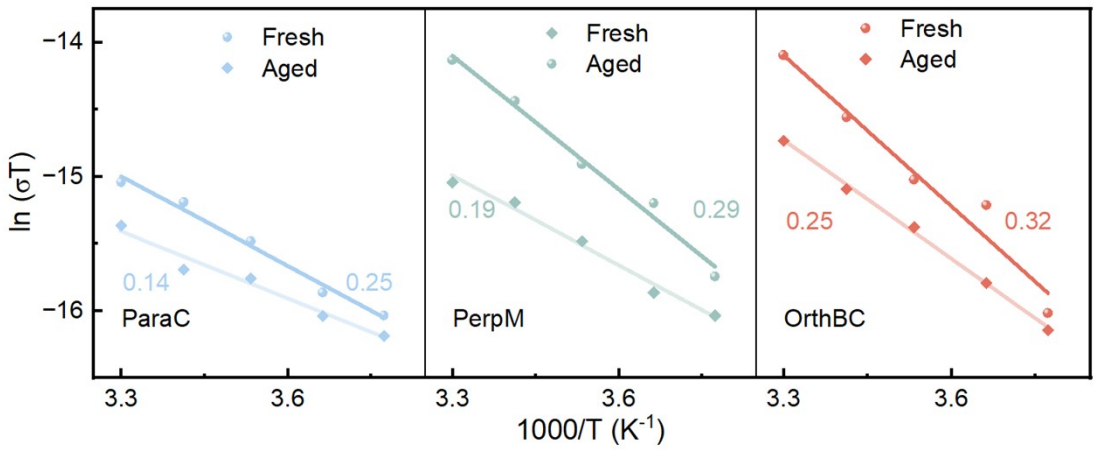


**Figure S29.** Nernst-Einstein plots of temperature-dependent conductivity for fresh and aged films, with the corresponding the $E_a$ for ion migration indicated.

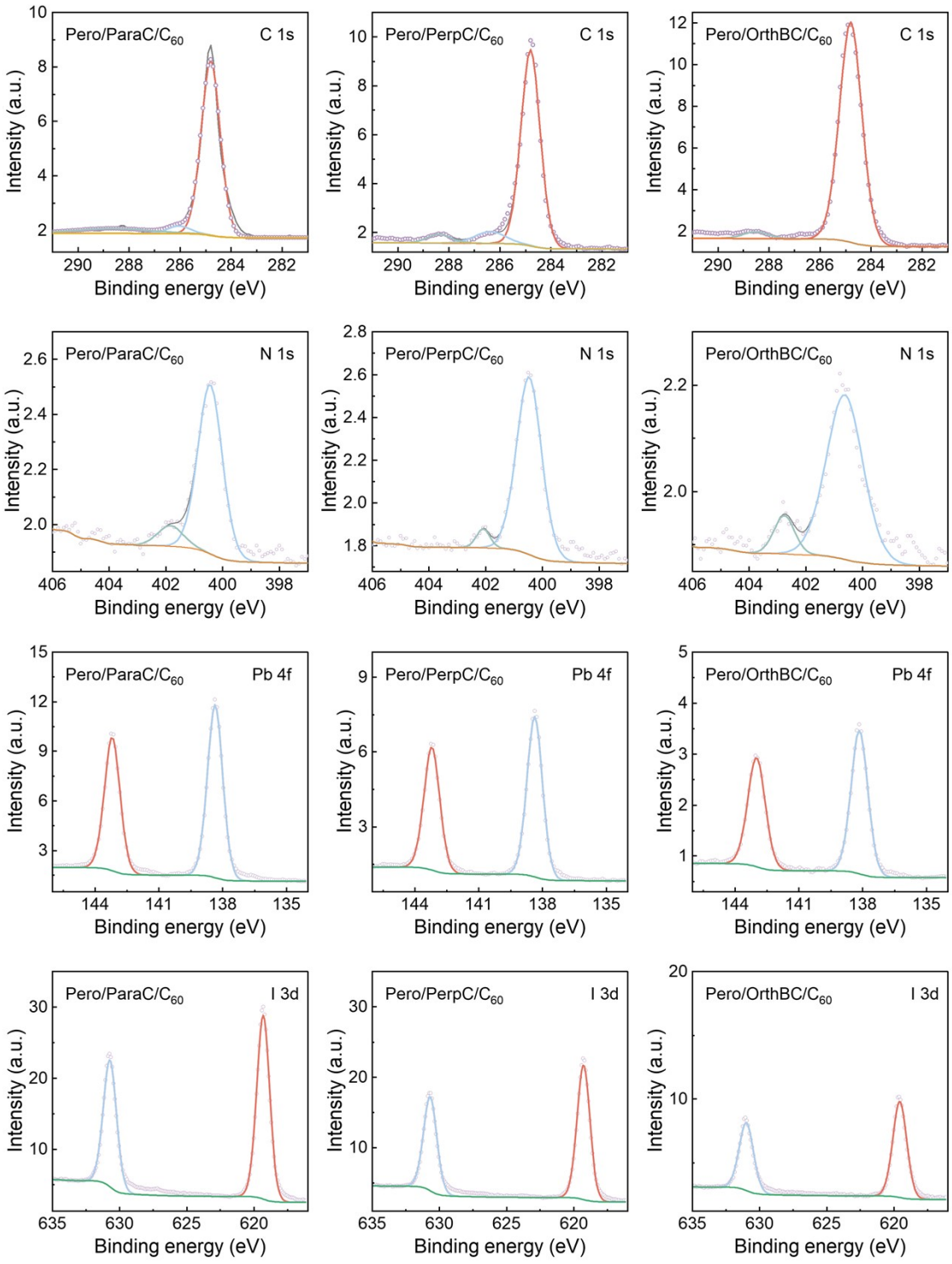


**Figure S30.** XPS core-level spectra of C 1s, N 1s, Pb 4f and I 3d for the perovskite/$C_{60}$ films with different passivation interlayers following thermal aging.

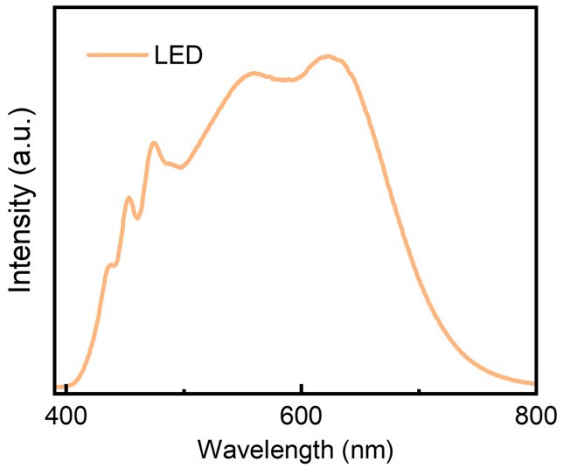


**Figure S31.** Spectral plot of the LED illumination for MPP tracking.

**Table S1.** The average chemical bond geometries (N–H···I length and angles) between amine groups and iodide ions.

| Condition | ParaC | | PerpC | | OrthBC | |
|---|---|---|---|---|---|---|
| | length (Å) | angle (°) | length (Å) | angle (°) | length (Å) | angle (°) |
| all | 3.01 ± 0.61 | 132.8 ± 19.5 | 2.78 ± 0.62 | 132.3 ± 17.5 | 2.99 ± 0.67 | 129.8 ± 20.6 |
| Strong N–H···I | 2.74 ± 0.44 | 143.3 ± 11.2 | 2.57 ± 0.28 | 137.0 ± 12.4 | 2.55 ± 0.44 | 143.5 ± 10.2 |

**Table S2.** XPS fitting peak positions of Pb 4f and I 3d in the pristine, ParaC, PerpC, and OrthBC-modified perovskite films.

| Condition | Pb $4f_{7/2}$ | Pb $4f_{5/2}$ | I $3d_{3/2}$ | I $3d_{5/2}$ |
|---|---|---|---|---|
| pristine | 137.91 | 142.80 | 618.83 | 630.29 |
| ParaC | 138.25 | 143.13 | 619.18 | 630.65 |
| PerpC | 138.21 | 143.09 | 619.07 | 630.53 |
| OrthBC | 138.32 | 143.20 | 619.27 | 630.75 |

**Table S3.** TRPL parameters of ParaC, PerpC, and OrthBC-modified perovskite films with $C_{60}$ and without $C_{60}$.

| Condition | $A_1$ (%) | $\tau_1$ (μs) | $A_2$ (%) | $\tau_2$ (μs) | $\tau_{avg.}$ (μs) |
|---|---|---|---|---|---|
| ParaC | 50.2 | 1.24 | 49. 8 | 5.52 | 3.37 |
| PerpC | 47.5 | 1.44 | 52.5 | 5.63 | 3.64 |
| OrthBC | 23.8 | 2.08 | 76.5 | 5.81 | 4.93 |
| ParaC/$C_{60}$ | 47.3 | 1.03 | 52.7 | 5.17 | 3.21 |
| PerpC/$C_{60}$ | 54.5 | 1.06 | 45.5 | 5.04 | 2.87 |
| OrthBC/$C_{60}$ | 62.1 | 0.95 | 37.8 | 4.89 | 2.44 |

**Table S4.** The PV performance parameters of the 0.09 $cm^2$ device fabricated via the antisolvent method.

| Condition | $V_{OC}$ (V) | $J_{SC}$ (mA $cm^{-2}$) | FF (%) | PCE (%) |
|---|---|---|---|---|
| ParaC | **1.162**<br>1.162 ± 0.002 | **25.80**<br>25.62 ± 0.22 | **83.94**<br>83.02 ± 0.64 | **25.16**<br>24.71 ± 0.3 |
| PerpC | **1.173**<br>1.171 ± 0.002 | **25.94**<br>25.75 ± 0.19 | **83.61**<br>83.04 ± 0.64 | **25.43**<br>25.03 ± 0.28 |
| OrthBC | **1.189**<br>1.183 ± 0.003 | **26.28**<br>26.03 ± 0.15 | **84.81**<br>84.05 ± 0.47 | **26.50**<br>25.89 ± 0.28 |

**Table S5.** The PV performance parameters of the 1-$cm^2$ devices.

| Condition | $V_{OC}$ (V) | $J_{SC}$ (mA $cm^{-2}$) | FF (%) | PCE (%) |
|---|---|---|---|---|
| ParaC | **1.144**<br>1.142 ± 0.004 | **25.21**<br>25.13 ± 0.17 | **79.52**<br>78.09 ± 0.76 | **22.93**<br>22.44 ± 0.38 |
| PerpC | **1.164**<br>1.162 ± 0.005 | **25.18**<br>24.95 ± 0.17 | **80.58**<br>78.58 ± 0.81 | **23.49**<br>22.79 ± 0.29 |
| OrthBC | **1.175**<br>1.176 ± 0.002 | **25.31**<br>25.4 ± 0.09 | **83.79**<br>82.5 ± 0.88 | **24.91**<br>24.65 ± 0.19 |

**Table S6.** Photovoltaic parameters highlighting the universal OrthBC strategy.

| Universality | Strategy | Molecules | $V_{OC}$ (V) | $J_{SC}$ (mA $cm^{-2}$) | FF (%) | PCE (%) |
|---|---|---|---|---|---|---|
| **OrthBC 1** | ParaC | PEAI | 1.144 | 25.71 | 81.54 | 23.98 |
| | PerpC | $PDAI_2$ | 1.165 | 25.40 | 81.60 | 24.15 |
| | OrthBC | PEAI-$PDAI_2$ | 1.177 | 25.60 | 84.25 | 25.39 |
| **OrthBC 2** | ParaC | APCl | 1.130 | 25.51 | 82.96 | 23.92 |
| | PerpC | $EDAI_2$ | 1.167 | 25.52 | 82.51 | 24.56 |
| | OrthBC | APCl-$EDAI_2$ | 1.178 | 25.67 | 83.02 | 25.11 |
| **OrthBC 3** | ParaC | APCl | 1.130 | 25.51 | 82.96 | 23.92 |
| | PerpC | $PDAI_2$ | 1.165 | 25.40 | 81.60 | 24.15 |
| | OrthBC | APCl-$PDAI_2$ | 1.176 | 25.72 | 82.81 | 25.04 |

**Table S7.** The PV performance parameters of the 0.09 $cm^2$ device were fabricated by sequential deposition.

| Condition | $V_{OC}$ (V) | $J_{SC}$ (mA $cm^{-2}$) | FF (%) | PCE (%) |
|---|---|---|---|---|
| ParaC | **1.148**<br>1.145 ± 0.006 | **25.75**<br>25.64 ± 0.11 | **83.36**<br>81.05 ± 1.32 | **24.67**<br>23.76 ± 0.54 |
| PerpC | **1.170**<br>1.163 ± 0.005 | **25.74**<br>25.44 ± 0.17 | **83.01**<br>82.48 ± 0.73 | **25.00**<br>24.41 ± 0.39 |
| OrthBC | **1.185**<br>1.177 ± 0.003 | **26.07**<br>25.65 ± 0.19 | **84.38**<br>83.47 ± 0.62 | **26.07**<br>25.43 ± 0.30 |

**Table S8.** Photovoltaic parameters of the device with a bandgap of 1.68 eV.

| Condition | $V_{OC}$ (V) | $J_{SC}$ (mA $cm^{-2}$) | FF (%) | PCE (%) |
|---|---|---|---|---|
| ParaC | **1.221**<br>1.217 ± 0.005 | **21.49**<br>21.07 ± 0.29 | **80.34**<br>78.96 ± 1.39 | **21.08**<br>19.77 ± 0.86 |
| PerpC | **1.234**<br>1.22 ± 0.004 | **21.85**<br>21.41 ± 0.14 | **82.71**<br>81.94 ± 0.64 | **22.31**<br>21.23 ± 0.69 |
| OrthBC | **1.264**<br>1.263 ± 0.007 | **22.23**<br>21.57 ± 0.32 | **85.70**<br>83.30 ± 0.1.13 | **24.07**<br>22.73 ± 0.61 |

**Table S9.** Reported photovoltaic parameters of 1.65-1.69 eV bandgap perovskite solar devices: literature vs. our work.

| Bandgap (eV) | Device structure | PCE (%) | $V_{OC}$ (V) | FF (%) | $J_{SC}$ (mA cm$^{-2}$) | Ref. |
|---|---|---|---|---|---|---|
| 1.68 | ITO/$NiO_x$/Me-2PACz/$Cs_{0.05}FA_{0.8}MA_{0.15}Pb(I_{0.76}Br_{0.24})_3$/OrthBC/$C_{60}$/BCP/Ag | **24.07** | 1.264 | 85.70 | 22.23 | Our work |
| 1.66 | FTO/$NiO_x$/BTSA/$Cs_{0.05}MA_{0.15}FA_{0.8}Pb(I_{0.76}Br_{0.24})_3$/$C_{60}$/BCP/Ag | **24.50** | 1.314 | 84.64 | 22.03 | [19] |
| 1.65 | ITO/MeO-2PACz/PTAA/$MHy_{0.05}Cs_{0.2}FA_{0.75}Pb(I_{0.82}Br_{0.15}Cl_{0.03})_3$/$C_{60}$/BCP/Cu | **23.30** | 1.28 | 83.8 | 21.8 | [20] |
| 1.67 | FTO/MeO-2PACz/$Cs_{0.05}(FA_{0.77}MA_{0.23})_{0.95}Pb(I_{0.77}Br_{0.23})_3$/MHI/PCBM/BCP/Ag | **23.25** | 1.28 | 83.06 | 21.87 | [21] |
| 1.67 | ITO/$NiO_x$/Me-4PACz/$Cs_{0.07}FA_{1.12}MA_{0.21}Pb(I_{0.77}Br_{0.23})_3$/$CF_3$-PEAI/LiF/$C_{60}$/BCP/Ag | **23.20** | 1.267 | 85.1 | 21.52 | [22] |
| 1.67 | /ITO/$NiO_x$/Me-4PACz/$Cs_{0.22}FA_{0.78}Pb(I_{0.85}Br_{0.15})_3$/$C_{60}$/BCP/Ag | **23.07** | 1.23 | 83.76 | 21.46 | [23] |
| 1.67 | ITO/4PADCB/$FA_{0.8}Cs_{0.15}MA_{0.05}PbI_{2.4}Br_{0.6}$/PDAI/$C_{60}$/BCP/Cu | **23.05** | 1.246 | 85.34 | 21.68 | [24] |
| 1.68 | ITO/$NiO_x$/MeO-2PACz/$Cs_{0.1}FA_{0.9}Pb(I_{0.83}Br_{0.17})_3$/$CF_3$-PEAI/$C_{60}$/BCP/Ag | **22.95** | 1.277 | 84.08 | 21.37 | [25] |
| 1.68 | ITO/2PACz/$Cs_{0.05}(FA_{0.77}MA_{0.23})_{0.95}Pb(I_{0.77}Br_{0.23})_3$/LiF/$C_{60}$/$SnO_2$/Ag | **22.87** | 1.24 | 84.67 | 21.76 | [26] |
| 1.68 | ITO/MeO-4PACz:$Nd^{3+}$/$Cs_{0.05}(FA_{0.77}MA_{0.23})_{0.95}Pb(I_{0.77}Br_{0.23})_3$/PEAI/$PC_{60}$BM/BCP/Ag | **22.82** | 1.212 | 86.35 | 21.8 | [27] |
| 1.68 | FTO/$NiO_x$/Me-4PACz/$Cs_{0.17}FA_{0.83}Pb(I_{0.83}Br_{0.17})_3$/$C_{60}$/$SnO_2$/Ag | **22.80** | 1.286 | 83.89 | 21.12 | [28] |
| 1.68 | ITO/$NiO_x$/MeO-2PACz/$Cs_{0.1}FA_{0.9}Pb(I_{0.83}Br_{0.17})_3$/$C_{60}$/BCP/Ag | **22.74** | 1.277 | 84.08 | 21.37 | [29] |
| 1.67 | ITO/4-PhCz/$Cs_{0.17}FA_{0.83}Pb(I_{0.8}Br_{0.2})_3$/$C_{60}$/BCP/Ag | **22.53** | 1.273 | 83.21 | 21.27 | [30] |
| 1.68 | ITO/$SnO_2$/$Cs_{0.05}(FA_{0.77}MA_{0.23})_{0.95}Pb(I_{0.77}Br_{0.23})_3$/PTAA/Au | **22.32** | 1.24 | 80.14 | 22.39 | [26] |
| 1.68 | ITO/MeO-2PACz/$Cs_{0.05}(FA_{0.77}MA_{0.23})_{0.95}Pb(I_{0.77}Br_{0.23})_3$/PCl/$C_{60}$/BCP/Ag | **22.30** | 1.254 | 85.6 | 20.3 | [31] |
| 1.68 | FTO/$NiO_x$/Me-4PACz/2DPAA/$Cs_{0.05}(FA_{0.77}MA_{0.23})_{0.95}Pb(I_{0.77}Br_{0.23})_3$/PDADI/$C_{60}$/BCP/Ag | **22.02** | 1.24 | 81.51 | 21.82 | [32] |
| 1.65 | ITO/$TiO_2$-$SnO_2$/$FA_{0.5}Cs_{0.5}Pb(I_{0.93}Br_{0.07})_3$/Spiro-OMeTAD/Ag | **21.94** | 1.27 | 82.36 | 20.99 | [33] |
| 1.67 | ITO/Poly-TPD/$Cs_{0.2}FA_{0.8}Pb(I_{0.82}Br_{0.15}Cl_{0.03})_3$/$C_{60}$/RPD-ITO/Ag | **21.80** | 1.242 | 82.57 | 21.26 | [34] |
| 1.69 | ITO/$NiO_x$/Me-4PACz/$Cs_{0.45}FA_{0.55}Pb(I_{0.85}Br_{0.15})_3$/$C_{60}$/$SnO_2$/Ag | **21.37** | 1.174 | 84.08 | 21.65 | [35] |
| 1.66 | FTO/Me-4PACz/$Cs_{0.24}FA_{0.76}Pb(I_{0.8}Br_{0.2})_3$/$C_{60}$/BCP/Ag | **20.10** | 1.201 | 80.6 | 20.76 | [36] |

**Table S10.** Atomic percentages and chemical bond ratios of perovskite films with different passivators, derived from XPS analysis.

| Condition | C-C (%) | C-N (%) | C=O (%) | N (%) | Pb (%) | I (%) |
|---|---|---|---|---|---|---|
| ParaC | 50.08 | 3.65 | 6.54 | 9.26 | 22.55 | 7.92 |
| PerpC | 46.98 | 4.07 | 7.84 | 11.47 | 22.29 | 7.35 |
| OrthBC | 51.06 | 3.34 | 5.41 | 10.44 | 22.33 | 7.42 |

**Table S11.** Surface atomic ratios of the perovskite/$C_{60}$ films with different passivation interlayers following thermal aging.

| | Area (CPS·eV) | | | | Atomic (%) | | | |
|---|---|---|---|---|---|---|---|---|
| | C 1s | N 1s | Pb 4f | I 3d | C 1s | N 1s | Pb 4f | I 3d |
| ParaC | 69991 | 7621 | 173239 | 543468 | 74.61 | 4.96 | 5.35 | 15.07 |
| PerpC | 87673 | 9808 | 107422 | 404448 | 81.69 | 5.60 | 2.90 | 9.80 |
| OrthBC | 121652 | 5752 | 51249 | 172788 | 92.75 | 2.69 | 1.13 | 3.42 |

**Table S12.** Performance and stability data of perovskite solar devices with molecular orientation passivation are derived from previous literature and this work.

| Architecture | PCE (%) | Molecular Orientation | Aging and Retention | Ref. |
|---|---|---|---|---|
| Inverted | 26.50 | OrthBC | ISOS-D-2: **93.9%**/1300 h<br>ISOS-L-2I, MPP: **91.2%**/1000 h | Our work |
| Inverted | 25.64 | ParaC | ISOS-D-2I: **80%**/900 h<br>ISOS-L-1I, MPP: **97%**/900 h | [5] |
| Inverted | 22.20 | ParaC | ISOS-D-1: **82%**/1250 h<br>ISOS-L-1I, MPP: **80%**/1200 h | [6] |
| Inverted | 24.20 | PerpC | ISOS-D-1: **64%**/192 h<br>ISOS-L-1, MPP: **92%**/240 h | [7] |
| Normal | 25.76 | ParaC | ISOS-D-1: **90.8%**/1000 h | [8] |
| Inverted | 25.45 | PerpC | ISOS-D-2: **90%**/1000 h<br>ISOS-L-1I, MPP: **100%**/3000 h | [9] |
| Inverted | 25.79 | ParaC | ISOS-D-1: **95%**/1200 h<br>ISOS-L-1I, MPP: **91%**/1200 h | [10] |
| Inverted | 24.08 | ParaC | ISOS-D-2I: **82%**/500 h<br>ISOS-L-1I, MPP: **95%**/500 h | [11] |
| Normal | 19.20 | PerpC | ISOS-D-2: **50%**/2880 h | [12] |
| Inverted | 24.87 | ParaC | ISOS-D-1I: **97%**/1800 h<br>ISOS-D-2I: **90%**/1200 h | [13] |
| Inverted | 26.32 | ParaC | ISOS-D-1: **90%**/1000 h<br>ISOS-L-1I, MPP: **95.8%**/2000 h | [14] |
| Inverted | 22.12 | ParaC | ISOS-D-1I: **95%**/1600 h<br>ISOS-L-1, MPP: **97%**/360 h | [15] |
| Inverted | 25.83 | PerpC | ISOS-D-1: **88%**/1000 h<br>ISOS-L-1I, MPP: **92%**/680 h | [16] |
| Normal | 24.70 | PerpC | ISOS-D-1: **95%**/1440 h | [17] |
| Inverted | 22.10 | PerpC | ISOS-D-1: **90%**/500 h<br>ISOS-L-1I: **80%**/750 h | [18] |

Note: ISOS-D-1: Dark storage at room temperature under ambient laboratory conditions. ISOS-D-2: Dark storage at 65 °C under ambient laboratory conditions. ISOS-L-1I: Continuous 1-sun illumination at room temperature. ISOS-L-2I: Continuous 1-sun illumination at 65 °C. The suffix "I" denotes testing in an inert environment. MPP refers to the maximum power point when a bias voltage is applied.

**Table S13.** A summary of the mixed-cation passivation or multifunctional strategies, underlying mechanisms, and the device performance.

| Year | Mechanism | Molecule 1 | Molecule 2 | PCE | Device Stability | Ref. |
|---|---|---|---|---|---|---|
| **2026** | **Orthogonal binary cation** | **Phenethylammonium iodide** | **Ethylenediamine dihydroiodide** | **26.50%**<br>**24.91%*** | **Retained 91.2% after 1000 h (ISOS-D-2)**<br>**Retained 93.9% after 1000 h (MPP, 65°C)** | **This work** |
| 2026 | Bimolecular co-anchoring strategy | 4-[3-(Trifluoromethyl)-3H-diazirin-3-yl]benzoic acid | 2-Benzamidinyl-5-guanidinopentanoic acid | 26.07% | Retained 95.0% after 1300 h (85°C)<br>Retained 91.0% after 1500 h (MPPT) | [37] |
| 2025 | Deprotonation-resistant passivation | N,N-Dimethylbenzenesulfonamide | Phenethylammonium iodide | 25.43% | Retained 96.1% after 1500 h (85°C) | [38] |
| 2024 | Phase-pure regulation | 3,6-Dimethyl-carbazole-9-ethylammonium iodide | m-Fluorophenylethylammonium iodide | 25.86%<br>25.08%* | Retained 90.0% after 1000 h (MPP) | [39] |
| 2024 | Molecular packing optimization | 4-tert-Butylbenzylammonium iodide | Phenylpropylammonium iodide | 26.00% | Retained 81.0% after 450 h (MPP) | [40] |
| 2024 | Kinetic competition control | Phenylmethylammonium iodide | Octylammonium iodide | 25.23% | Retained 88.0% after 1000 h (MPP) | [41] |
| 2023 | Ion-diffusion management | Octylammonium iodide | Guanidinium chloride | 25.43% | Retained 83.0% after 1200 h (MPP) | [42] |
| 2023 | Chemical and field-effect passivation | Propane-1,3-diammonium iodide | 3-(Methylthio)propylamine hydroiodide | 25.10% | Retained stability for >2000 h (65°C) | [43] |

Note: *Device with 1.00 $cm^2$; ISOS: International Summit on Organic Photovoltaic Stability; ISOS-D-2: dark storage at 65°C; ISOS-L-2I: light soaking at 65°C; MPP: maximum power point.

## References:


1 J. Guo, B. Wang, D. Lu, T. Wang, T. Liu, R. Wang, X. Dong, T. Zhou, N. Zheng, Q. Fu, Z. Xie, X. Wan, G. Xing, Y. Chen and Y. Liu, *Adv. Mater.*, 2023, **35**, 2212126.

2 C. Shao, J. Ma, G. Niu, Z. Nie, Y. Zhao, F. Wang and J. Wang, *Adv. Mater.*, 2025, **37**, 2417150.

3 Z. Li, X. Sun, X. Zheng, B. Li, D. Gao, S. Zhang, X. Wu, S. Li, J. Gong, J. M. Luther, Z. Li and Z. Zhu, *Science*, 2023, **382**, 284–289.

4 L. Krückemeier, U. Rau, M. Stolterfoht and T. Kirchartz, *Adv. Energy Mater.*, DOI:10.1002/aenm.201902573.

5 G. Li, Z. Gao, G. Huang, J. He, K. Sun, X. Wang, H. Wu, C. Gao, X. Zeng, X. Zhou, H. Hu, Y. Hu, Q. Bai, T. Shan, C. Xie, Y. Wang, G. Zhang, M. Qiu, P. Han, S. Li and P. You, *Chem. Eng. J.*, 2025, **516**, 163955.

6 J. Liu, Y. He, L. Ding, H. Zhang, Q. Li, L. Jia, J. Yu, T. W. Lau, M. Li, Y. Qin, X. Gu, F. Zhang, Q. Li, Y. Yang, S. Zhao, X. Wu, J. Liu, T. Liu, Y. Gao, Y. Wang, X. Dong, H. Chen, P. Li, T. Zhou, M. Yang, X. Ru, F. Peng, S. Yin, M. Qu, D. Zhao, Z. Zhao, M. Li, P. Guo, H. Yan, C. Xiao, P. Xiao, J. Yin, X. Zhang, Z. Li, B. He and X. Xu, *Nature*, 2024, **635**, 596–603.

7 G. Ren, Z. Zhang, Y. Deng, Z. Li, C. Liu, M. Wang and W. Guo, *Energy Environ. Sci.*, 2023, **16**, 565–573.

8 J. Chen, K. Huang, W. Peng, J. Tang, Y. Dai, Z. Li, L. Hao, X. Zhou, B.-B. Yu, R. Xu, H. Dong, X. Wang and C. Liu, *Nano Energy*, 2025, **145**, 111441.

9 H. Xu, Z. Liang, J. Ye, Y. Zhang, Z. Wang, H. Zhang, C. Wan, G. Xu, J. Zeng, B. Xu, Z. Xiao, T. Kirchartz and X. Pan, *Energy Environ. Sci.*, 2023, **16**, 5792–5804.

10 W. Gao, J. Ding, Q. Ma, H. Zhang, J. Zhang, Z. Zhang, M. Li, Y. Wang, B. Zhang, T. Pauporté, J. Tang, J. Chen and C. Chen, *Adv. Mater.*, 2025, **37**, 2413304.

11 J. Liu, J. Chen, L. Xie, S. Yang, Y. Meng, M. Li, C. Xiao, J. Zhu, H. Do, J. Zhang, M. Yang and Z. Ge, *Angew. Chem. Int. Ed.*, 2024, **63**, e202403610.

12 F. Wang, W. Geng, Y. Zhou, H. Fang, C. Tong, M. A. Loi, L. Liu and N. Zhao, *Adv. Mater.*, 2016, **28**, 9986–9992.

13 X. Xu, Q. Du, H. Kang, X. Gu, C. Shan, J. Zeng, T. Dai, Q. Yang, X. Sun, G. Li, E. Zhou, G. Luo, B. Xu and A. K. K. Kyaw, *Adv. Funct. Mater.*, 2024, **34**, 2408512.

14 M. Lu, J. Ding, Q. Ma, Z. Zhang, M. Li, W. Gao, W. Mo, B. Zhang, T. Pauporté, J. Zhang, Y. Wang, J.-X. Tang, J. Chen and C. Chen, *Energy Environ. Sci.*, 2025, **18**, 5973–5984.

15 Z. Liu, P. Wang, Y. Gao, X. Ge, Y. Luo, X. Du, S. Xu, B. Shi, S. Liu, Y. Zhao and X. Zhang, *Adv. Funct. Mater.*, 2025, 2510444.

16 I. Ullah, J. Guo, B. Wang, C. Guo, Z. Tang, J. Shi, X. Ling, W. Ma and J. Yuan, *Adv. Funct. Mater.*, 2025, e10400.

17 C. Liu, P. Shi, C. Li, W. Huang, X. Yang, I. Yavuz, J. Xue, R. Liu and R. Wang, *ACS Sustain. Chem. Eng.*, 2024, **12**, 8923–8929.

18 Z. Xing, M.-W. An, Z.-C. Chen, M. Hu, X. Huang, L.-L. Deng, Q. Zhang, X. Guo, S.-Y. Xie and S. Yang, *J. Am. Chem. Soc.*, 2022, **144**, 13839–13850.

19 J. Ding, Y. Liao, H. Liu, Y. Ding, Q. Ma, M. Li, Z. Zhang, J. Zhang, J.-X. Tang, J. Sheng, J. Chen and C. Chen, *Nat. Commun.*, 2025, **16**, 8407.

20 G. Yang, H. Gu, J. Yin, C. Fei, Z. Shi, X. Shi, X. Ying and J. Huang, *Nat. Sustain.*, 2025, **8**, 456–463.

21 Y. Yang, Q. Chang, J. Su, L. Chao, Y. Wang, Z. Dai, X. Huang, S. Nie, P. Guo, J. Yin, Z. Liu, Y. Lin, A. K. -Y. Jen, R. Chen and H. Wang, *Adv. Mater.*, 2025, **37**, 2416513.
22 L. Tian, E. Bi, I. Yavuz, C. Deger, Y. Tian, J. Zhou, S. Zhang, Q. Liu, J. Shen, L. Yao, K. Zhao, J. Xu, Z. Chen, L. Xiao, Z. Yang, P. Shi, X. Zhang, S. Wang, S. Chu, M. Haider, J. Xue and R. Wang, *Nat. Photonics*, 2025, **19**, 479–485.
23 L. Yang, S. Wang, N. Ma, W. Shi, Z. Fang, Y. Jin, E. Hou, P. Xu, F. Cao, W. Li, K. Gao, Y. Li, D. Cao, S. Yang, C. Yu, L. Xie, X. Yang and Z. Wei, *Angew. Chem.*, 2025, e202500350.
24 S. Wu, M. Hu, J. Wang, J. Zhu, W. Jiao, Z. Wu, Z. Song, Y. Luo, J. You, Y. Xu, Z. Gao, Z. Zhang, J. Qu, P. Jiang, X. Hao, S. Ren, C. Chen and D. Zhao, *Adv. Mater.*, 2025, **37**, 2503269.
25 L. Wang, N. Wang, X. Wu, B. Liu, Q. Liu, B. Li, D. Zhang, N. Kalasariya, Y. Zhang, X. Yan, J. Wang, P. Zheng, J. Yang, H. Jin, C. Wang, L. Qian, B. Yang, Y. Wang, X. Cheng, T. Song, M. Stolterfoht, X. C. Zeng, X. Zhang, M. Xu, Y. Bai, F. Xu, C. Zhou and Z. Zhu, *Adv. Mater.*, 2025, **37**, 2416150.
26 Y. Yao, B. Li, D. Ding, C. Kan, P. Hang, D. Zhang, Z. Hu, Z. Ni, X. Yu and D. Yang, *Nat. Commun.*, 2025, **16**, 40.
27 M. Zhou, Z. Xie, Y. Han, G. Wang, X. Chang, Y. Zhu, K. Li, N. Fan, H. Wang, X. Zhu, J. Chen and T. Zhu, *Small*, 2025, **21**, 2411637.
28 T. Ye, L. Qiao, T. Wang, P. Wang, L. Zhang, R. Sun, W. Kong, M. Xu, X. Yan, J. Yang, X. Zhang and X. Yang, *Adv. Funct. Mater.*, 2025, 2419391.
29 J. Li, S. Zhu, C. Yin, C. Chen, J. Yuan, H. Zhao, H. Gong, B. Yang, D. Zheng, G. Xing, D. Zhao, J. Yu and S. Bai, *Adv. Funct. Mater.*, 2025, 2422175.
30 C. Guo, H. Du, Y. Wang, X. Gao, Y. Lan, Y. Xiao, W. Jiang, Y. Zhou, Q. Yuan, Z. Qiang, J. Zheng, L. Yang, C. Wang, N. Yang, R. Lin, G. Liang, M. U. Rothmann, X. Ouyang, Y. Cheng and W. Li, *Adv. Mater.*, 2025, 2504520.
31 X. Li, Z. Ying, S. Li, L. Chen, M. Zhang, L. Liu, X. Guo, J. Wu, Y. Sun, C. Xiao, Y. Zeng, J. Wu, X. Yang and J. Ye, *Nano-Micro Lett.*, 2025, **17**, 141.
32 Y. Peng, Y. Chen, J. Zhou, C. Luo, W. Tang, Y. Duan, Y. Wu and Q. Peng, *Nat. Commun.*, 2025, **16**, 1252.
33 L. Han, X. Feng, Z. Shao, G. Wu, C. Bi, X. Huang, X. Du, Q. Meng, Y. Han, L. Lyu, R. Liu, C. Cui, Y. Li, H. Wei, Z. Wu, B. Lu, Y. Zhang, S. Pang and G. Cui, *ACS Energy Lett.*, 2025, **10**, 1321–1329.
34 W. Li, X. Liu, J. Zhang, H. Wang, C. Yuan, S. Lin, C. Chen, C. Shen, J. Tang, J. Li, T. Bu, S. Wang, Y. Jiang, X. Xiao and J. Gong, *Adv. Mater.*, 2025, **37**, 2417094.
35 Z. Dong, J. Hu, X. Guo, Z. Shi, H. Chen, Y. Wang, R. Luo, J. A. Steele, Z. Degnan, E. Solano, Q. Zhou, N. Kalasariya, N. Li, T. Wang, J. Chen, L. K. Lee, Y. Wang, J. Li, M. Stolterfoht, M. Sui, Y. Lu and Y. Hou, *Nat. Mater.*, DOI:10.1038/s41563-025-02375-8.
36 Y. Dou, C. Geng, C. Duan, S. Hu, X. Deng, Y. Chen, A. Kong, Y. Peng, Z. Qiang and Z. Ku, *Nano Energy*, 2025, **139**, 110914.
37 Y. Wang, L. Zhang, K. Li, Y. Wang, Y. Tao, X. Lu, S. Tsang, H. Kuo, J. You, A. K. Y. Jen and S. F. Liu, *Adv. Energy Mater.*, 2026, **16**, e04844.
38 B. Kang, B. Koo, H. J. Park, W. Kim, Y. Yoo, J. Kim, S. Bae, M. J. Ko, P. Lee and H. Jung, *Adv. Energy Mater.*, 2026, **16**, e03429.
39 Z. Shi, S. Liu, R. Luo, J. Ma, H. Tian, X. Wang, Z. Dong, X. Guo, J. Chen, J. Feng, C. Xiao, Y. Wu, W. Hu and Y. Hou, *J. Am. Chem. Soc.*, 2025, **147**, 1055–1062.

40 Z. Qu, Y. Zhao, F. Ma, L. Mei, X.-K. Chen, H. Zhou, X. Chu, Y. Yang, Q. Jiang, X. Zhang and J. You, *Nat. Commun.*, 2024, **15**, 8620.
41 Y. Ma, F. Li, J. Gong, L. Wang, X. Tang, P. Zeng, P. F. Chan, W. Zhu, C. Zhang and M. Liu, *Energy Environ. Sci.*, 2024, **17**, 1570–1579.
42 L. Shen, P. Song, L. Zheng, L. Wang, X. Zhang, K. Liu, Y. Liang, W. Tian, Y. Luo, J. Qiu, C. Tian, L. Xie and Z. Wei, *Adv. Mater.*, 2023, **35**, 2301624.
43 C. Liu, Y. Yang, H. Chen, J. Xu, A. Liu, A. S. R. Bati, H. Zhu, L. Grater, S. S. Hadke, C. Huang, V. K. Sangwan, T. Cai, D. Shin, L. X. Chen, M. C. Hersam, C. A. Mirkin, B. Chen, M. G. Kanatzidis and E. H. Sargent, *Science*, 2023, **382**, 810–815.